Granular Matter (2015) 17:197–216
DOI 10.1007/s10035-015-0552-6

ORIGINAL PAPER

Analysis of bender element test interpretation using the discrete element method

J. O'Donovan · C. O'Sullivan · G. Marketos · D. Muir Wood

Received: 14 June 2014 / Published online: 13 March 2015

Abstract While bender element testing is now well-established as a laboratory technique to determine soil stiffness, a robust technique to interpret the data remains elusive. A discrete element method (DEM) model of a face-centred cubic packing of uniform spheres was created to simulate bender element tests to investigate this test from a fundamental perspective. During the DEM simulations transmitter and receiver signals were recorded, analogous to the data available in laboratory tests, and these macro-scale data were supplemented with particle scale measurements (forces, stresses and displacements). A range of approaches previously applied in experimental and numerical studies were used to analyse the resulting data in both the time and frequency domains. The shortcomings in these approaches are clear from the differences in the resultant shear stiffness values and the frequency-dependent nature of the values. The particle-scale data enabled visualization of the passage of the wave through the sample, and it was found not to be possible to precisely link the arrival of the shear wave at the receiver and any of the previously proposed characteristic points along the signal recorded at the receiver. The most reliable determination of the shear wave velocity was obtained by applying a two-dimensional fast Fourier transform (2D FFT) to the data describing the velocity of the particles lying between the transmitter and receiver elements. Use of the DEM model and this 2D FFT approach facilitated the sensitivity of the system response to small variations in the interparticle force–displacement law (the contact model) to be established.

Keywords DEM · Wave propagation · Small-strain stiffness · Contact model

J. O'Donovan (✉)
Ground Engineering Buro Happold, 17 Newman St., London W1T 1PD, UK
e-mail: j.odonovan09@alumni.imperial.ac.uk

C. O'Sullivan
Department of Civil and Environmental Engineering, Imperial College London, South Kensington, London SW6 2AZ, UK

G. Marketos
School of Geosciences, Utrecht University, 3584 CD Utrecht, The Netherlands

D. Muir Wood
Division of Civil Engineering, University of Dundee, Dundee DD1 4HN, UK

1 Introduction

The use of bender elements to estimate small strain stiffness of soils in the laboratory is now well established (e.g. [1,2]). As originally proposed by Shirley and Hampton [3], a bender element is formed from two pieces of piezoceramic material. These are glued together and given electrical connections such that when a voltage is applied one piece becomes shorter and the other longer, due to the piezoelectric effect, and the combination is forced to bend. Referring to Fig. 1, if a bender element is inserted into the face of a soil sample then the flexural deformation induces a motion at the free end of the element and this induces a shear wave in the soil itself. This disturbance then travels through the sample and induces flexural deformation of a second bender element (the receiver), in turn generating a voltage. It is the transverse displacement of the bender tips, relative to the direction of energy propagation that gives the generation and measurement of shear waves. Shirley and Hampton, and many subsequent researchers, have acknowledged that the transmitter element generates compression as well as shear waves inside the soil sample,

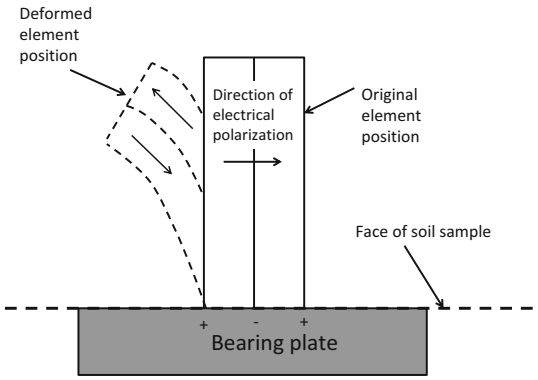

Fig. 1 Schematic diagram of bender element

and there is as yet no consensus as to what approach should be adopted to identify the precise arrival time for the shear wave based upon the voltage recorded at the receiver element.

Various interpretation methods have been proposed to determine this travel time, t_{arr}, such as Yamashita et al. [4], da Fonseca et al. [5] and Yang and Gu [2]. Using t_{arr} and knowing the sample dimensions a shear wave velocity, V_s, can be determined and (assuming the material to be continuous and linear elastic) the shear stiffness is calculated as $G = \rho V_s^2$, where ρ is the sample density. The signals recorded at the receiver bender element are, however, highly complex and accurate identification of the arrival time is non-trivial. The complexity induces a subjectivity in the bender element test interpretation and so the accuracy of estimates of G obtained via bender element tests has been questioned (e.g. [2,6], and [4]). Arroyo et al. [7] compared a variety of time and frequency domain bender element interpretative approaches experimentally and concluded that the global uncertainty in moduli determination may be as much as 100 %. Leong et al. [8] measured the shear wave speed resulting from waves transmitted at different frequencies and found an uncertainty in the speed of up to 17 %. Furthermore, the results of Marketos and O'Sullivan [9] indicate that the shear wave arrival could not be linked to any point based on the time-domain arrangements of signals for simplified two-dimensional arrangements of particles. Planar shear piezo-transducers that contact the soil sample face without penetration have also been used to measure shear wave velocity (e.g. Khidas and Jia [10] and Suwal and Kuwano [11]). However, bender elements, which penetrate the sample face and generate point sources of waves are the dominant type of shear piezo transducer used in commercial and research-based soil mechanics tests. The challenges associated with interpreting data from bender elements that are embedded in the samples and considered to generate point source disturbances are the prime motivation for the fundamental examination of the response of a relatively simple granular material to a point source excitation presented here.

Previous researchers including Hazzard et al. [12], Li and Holt [13], Mouraille et al. [14] and Xu et al. [15] have demonstrated the application of the discrete element method (DEM) to study wave propagation in granular media. Here these earlier studies are extended by using DEM to consider the response of a granular material to a point source excitation, analogous to a bender element. A regular assembly of uniform spheres is used to enable consideration of a system that is slightly simpler than a real, random, polydisperse material. O'Donovan et al. [16] and Gu and Yang [17] demonstrated that significant insight can be obtained by considering the response of an idealized system. This current paper builds upon the simulations carried out in [14] and extends them to a larger three-dimensional sample. The analysis carried out in [14] is applied to the three-dimensional sample and novel interpretation and frequency domain techniques are presented here. The effects of interparticle contact models and boundary conditions can be observed in a controlled manner. In principle, the DEM data set enables the shear wave progression through the sample to be monitored in both time and frequency domains and consequently the shear wave arrival at the receiver can be accurately identified. Furthermore the basis of the testing approach can be interrogated without the need to consider the mechanics of the physical test, i.e. details of wiring and other issues summarized by da Fonseca et al. [5].

The research described here seeks to address two key questions (1) how can we reliably estimate shear stiffness using point source transmitters and receivers and (2) using this reliable interpretive technique, how does the DEM contact model affect the stiffness? This stiffness is the stiffness of a particulate assembly and is the macro scale constitutive law governing the deformation of a granular sample produced from an applied stress. The paper firstly outlines the simulation approach adopted and then discusses the system response to the propagation of the stress wave through the specimen. Arrival time, t_{arr}, values determined by analysing the system response and using theoretical approaches are compared with t_{arr} values obtained using conventional laboratory-based interpretation approaches. The most reliable stiffness estimates are shown to be obtained by using the particle-scale data and applying a two-dimensional fast Fourier transform (2D FFT). This 2D FFT method is then used to explore the sensitivity of the relationship between confining pressure and stiffness to the force–displacement relationship assumed at the particle contacts.

2 Simulation approach

The data considered here were generated via three-dimensional DEM simulations. As indicated in Fig. 2, the specimen considered contained 81,576 particles, each

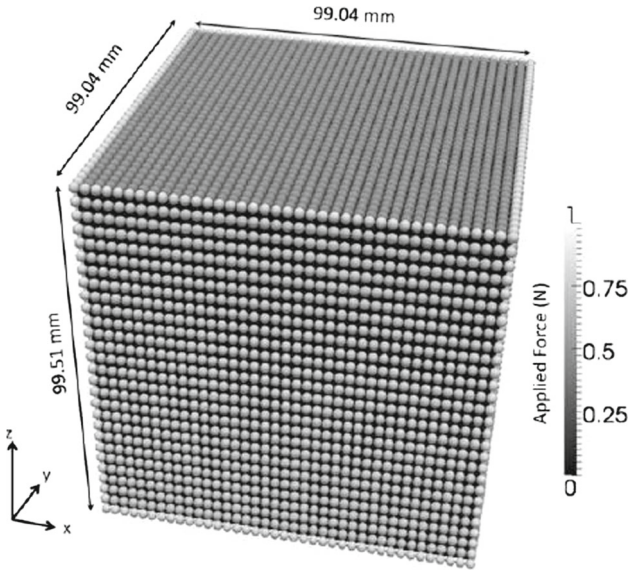

Fig. 2 Sample layout—magnitude of applied forces illustrated via shading

Table 1 Properties of the particles used in the DEM simulations

Diameter, d	2.54 mm
Density, ρ_{part}	2.23 g/mm^3
Shear modulus, G_{part}	16.67 GPa
Friction coefficient	0.088
Poisson's ratio, ν	0.20
Hardness, H_{part}	1.50 GPa
Roughness, RMS_{fpart}	0.10 μm

2.54 mm in diameter, in a face-centred-cubic (FCC) packing with dimensions of 99.04 mm in the x- and y-directions and 99.51 mm in the z-direction. This packing configuration has been previously used by Mouraille et al. [14], Rowe [18], Thornton [19], Mouraille and Luding [20] and Santamarina and Cascante [21]: the latter three describe small-strain and dynamic response. The cubic anisotropy of this packing requires three parameters to develop the stiffness tensor: a Young's modulus, a Poisson's ratio and an independent shear modulus [22].

The PFC3D code, [23], was used. PFC3D uses the DEM algorithm as originally proposed by Cundall and Strack [24] and Cundall and Strack [25]. Most of the simulations in this paper used the simplified Hertz–Mindlin (HM) contact model that is implemented in this code. The particle properties are representative of boro-silicate glass ballotini and are listed in Table 1; see [26] for more information on how these properties were measured. The HM model assumes smooth particle surfaces. The contact model used during simulation of the wave generation and propagation included a viscous dashpot with damping coefficient of 0.01. In this study all particles had the same properties.

In the HM model, Hertzian theory is used to formulate a non-linear elastic DEM contact model in the normal direction. The model parameters are the particle shear modulus, $G_{particle}$, the particle Poisson's ratio, $\nu_{particle}$, and the particle radius, $R_{particle}$. Knowing the particle shear modulus and Poisson's ratio the particle Young's modulus, $E_{particle}$, was calculated. In developing his theory, Hertz considered the circular contact area, a, that develops between two contacting spheres. As the overlap, α, between the two particles increases the contact area also increases resulting in a non-linear force-displacement relationship at the contact. Referring to [27] and [28] the relevant equations are as follows where the subscripts 1 and 2 refer to the two particles in contact and k^n is the interparticle contact stiffness in the normal direction:

$$k^n = 2E^* a \tag{1}$$

where

$$\frac{1}{E^*} = \frac{1-\nu_1^2}{E_1} + \frac{1-\nu_2^2}{E_2} \tag{2}$$

$$a = \sqrt{R^* \alpha} \tag{3}$$

and

$$\frac{1}{R^*} = \frac{1}{R_1} + \frac{1}{R_2} \tag{4}$$

A limited number of the simulations used a Cavarretta Mindlin (CM) model, in the normal direction, which follows the contact relationship described by Cavarretta et al. [29]. This model considers the influence of plasticity of the real particle surfaces and takes as additional inputs the grain roughness (RMS_f) and the hardness ($H_{particle}$), see Table 1. The load–displacement relationships for the CM and Hertzian normal contact models are shown in Fig. 3a.

The displacement above which the contact area is large enough to exhibit some Hertzian elastic behaviour, α_p, is given by the following equation:

$$\alpha_p = \frac{9R^*\pi^2}{16}\left(\frac{H_{particle}}{E^*}\right)^2 \tag{5}$$

P_{GT} is the threshold force above which the contact behaviour becomes fully Hertzian and given by:

$$P_{GT} \cong 100(RMS_f)E^*[2R^*(RMS_f)]^{0.5} \tag{6}$$

The overlap at which the force is equal to P_{GT} is α_{GT}:

$$\alpha_{GT} = \left(\frac{3P_{GT}}{4\sqrt{R^*}E^*}\right)^{2/3} \tag{7}$$

For the elastic version the entire force-displacement model can be expressed as follows:

$$P = P_{GT}\alpha_{GT}^{-b}\alpha^{b} \qquad \alpha < \alpha_{GT} \tag{8a}$$

$$P = \frac{4}{3}\sqrt{R^*}E^*(\alpha - \alpha_{GT})^{3/2} \qquad \alpha \geq \alpha_{GT} \tag{8b}$$

In Eq. 8 the exponent, b, is:

$$b = 2E^*[R^*(\alpha_{GT} - \alpha_p)]^{0.5}\alpha_{GT}P_{GT}^{-1} \tag{9}$$

Two tangential contact models were considered. For the HM and CM models the simplified Mindlin tangential model was used so that

$$\Delta k_t = 8G^*a \tag{10}$$

where G^* is given by

$$\frac{1}{G^*} = \frac{2 - \nu_{particle\_1}}{G_{particle\_1}} + \frac{2 - \nu_{particle\_2}}{G_{particle\_2}} \tag{11}$$

and the incremental tangential force is $\Delta T = \Delta k_t \Delta\delta$. The Hertz–Mindlin–Deresiewicz (HMD) model is based upon the work of Mindlin and Deresiewicz [30] and its implementation in DEM was discussed by Thornton and Randall [27] and Thornton and Yin [28]. The HMD model dissipates energy due to friction using the theory of micro-slip at the contact surface (refer to [27] and [31]). The model requires the same input parameters as are used in the Hertz–Mindlin force–displacement model. Figure 3b compares the Mindlin–Deresiewicz tangential contact model with the simplified Mindlin tangential contact model. In the HMD model the tangential stiffness, k^t, is given by:

$$k^t = 8G^*\theta a \pm \mu(1-\theta)\frac{\Delta P}{\Delta\delta} \tag{12}$$

where G^* is given by Eq. 11 and

$$\theta^3 = 1 - \frac{T + \mu\Delta P}{\mu P} \quad \text{(loading)} \tag{13a}$$

$$\theta^3 = 1 - \frac{T^* - T + 2\mu\Delta P}{2\mu P} \quad \text{(unloading)} \tag{13b}$$

$$\theta^3 = 1 - \frac{T - T^{**} + 2\mu\Delta P}{2\mu P} \quad \text{(reloading)} \tag{13c}$$

$\Delta\delta$ = the change in tangential displacement, T^* = load reversal point where the tangential displacement starts to unload, T^{**} = load reversal point where the tangential displacement starts to reload and the negative sign in the first equation is only invoked during unloading.

Irrespective of the contact model used, each sample was isotropically compressed to a specified isotropic stress using rigid walls. During simulation of the wave propagation, the boundary conditions were stress-controlled and, as in [25], a force was applied to each boundary particle to obtain the specified confining stress. This boundary condition is well understood and captures the effect of a flexible boundary by applying a constant stress boundary and allowing particles on the outside of the sample to displace. Although the inertia of the confining fluid, which in this case is air, is not modelled it is likely to have a negligible effect in comparison to the pressure applied from the confinement of the fluid. Simulation of the bender element insertion would have disturbed the ideal packing and compromised comparison with the analytical solutions described below. Following the prior two-dimensional simulations of [16], both the transmitter and receiver elements were simulated using individual particles. This approach has the advantage of isolating the dynamic response of the sample; the dynamic response of the

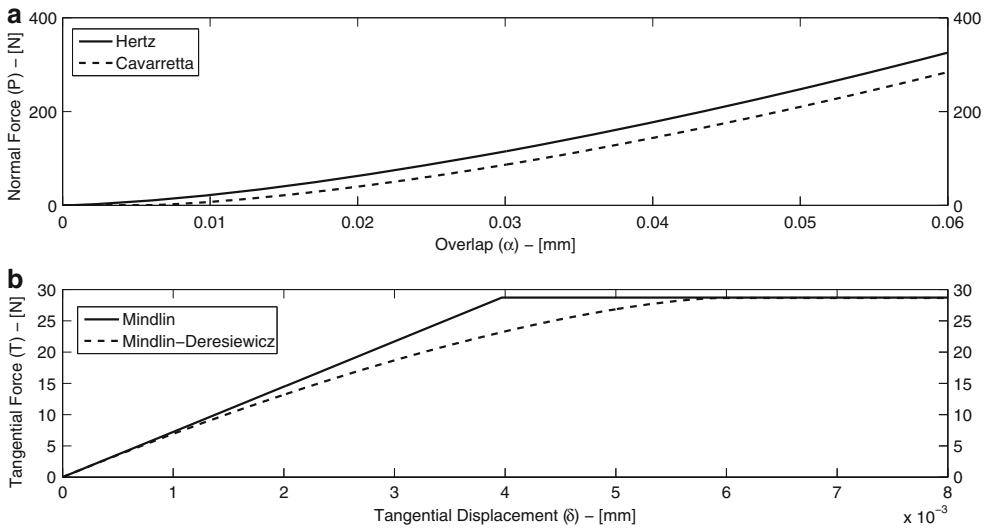

Fig. 3 **a** Comparison of Hertz and Cavarretta normal direction contact models with no change in tangential force and tangential displacement. **b** Comparison of Mindlin and Mindlin–Deresiewicz tangential direction contact models with no change in normal force or in tangential loading direction

bender element and the bender-soil interaction are excluded. Here, the transmitter was located in the middle of one face of the sample one layer in from the boundary (i.e. centred at x = 2.55 mm) and the receiver was located mid-way along the opposite face of the sample (i.e. centred at x = 96.51 mm), again one layer in from the boundary. The bender element tests were simulated by imposing a controlled translational displacement on the transmitter particle in the y-direction. The centre-centre distance (91.5 mm) was taken to be the travel distance in the x-direction for the shear (s-) waves. The shear wave velocity is denoted V_{xy}, i.e. the velocity of a wave travelling in the x-direction and polarized in the y-direction, with the corresponding stiffness being G_{xy}. The input signal was a single period sine pulse as has been used in the recent experimental studies of [2] amongst many others.

3 System response in time domain

Figure 4 presents the transmitted and received signals for a typical bender element test simulation, in each the displacement values plotted are normalized by the maximum displacement recorded for the relevant element (transmitter or receiver). The sample was confined isotropically at 100 kPa and the simplified Hertz–Mindlin contact model (HM) was used. The transmitted signal was a single period sine wave with frequency of 30 kHz and amplitude of 0.000125 mm. The frequency selected is similar to the frequencies used in experimental studies such as [2] and [32]. The resultant number of full shear wavelengths that occur between the transmitting bender element and the receiving bender element is $R_d = 5.63$. This exceeds the minimum R_d values advised by Hardy [33] ($R_{d,min} = 4$) and Arroyo et al. [7] ($R_{d,min} = 1.6$) but not that advised by Jovičić et al. [34] ($R_{d,min} = 8$); the value proposed by Jovičić may be on the conservative side. The ratio of wavelength to median particle diameter (i.e. λ/d_{50}) was 6.40, and this exceeds the minimum value of 2 that is the theoretical lower bound of λ/d_{50} for a wave that propagates further than one particle [35]:

$$k_{\max} = \frac{\pi}{\Delta x} \tag{14}$$

where k_{max} is the maximum wavenumber of the propagating waves and Δx is the separation between two consecutive particles (approximately the particle diameter, d). λ is equal to $2\,\pi/k$ and, therefore, λ_{min} equals $2d$. The displacement amplitude was chosen via a parametric study to minimize the change in contact configuration and hence avoid one potential source of non-linearity. It was impossible to avoid all contact slippages and, as detailed in [36], sliding was induced in about 8 contacts close to the transmitter.

Observation of the raw received signal in the time domain gives initial insight into the system response. The plot in Fig. 4 is normalised as the received wave was much lower amplitude than the transmitted wave. The reduction in amplitude is caused by geometrical spreading of the energy and scattering (including mode conversion). A near field effect (see [37] and [38]) is observed as initial small amplitude fluctuations on the received signal prior to the main shear wave arrival. The frequency of the received signal oscillations is different to the transmitted signal oscillations indicating dispersion. This demonstrates that the regular lattice packing of grains has reproduced some but not all of the complexities present in the received signals from laboratory experiments. This highlights its use as a tool which can be compared with existing analytical work in an effort to explain the sources of these complexities. Many of these complexities remain

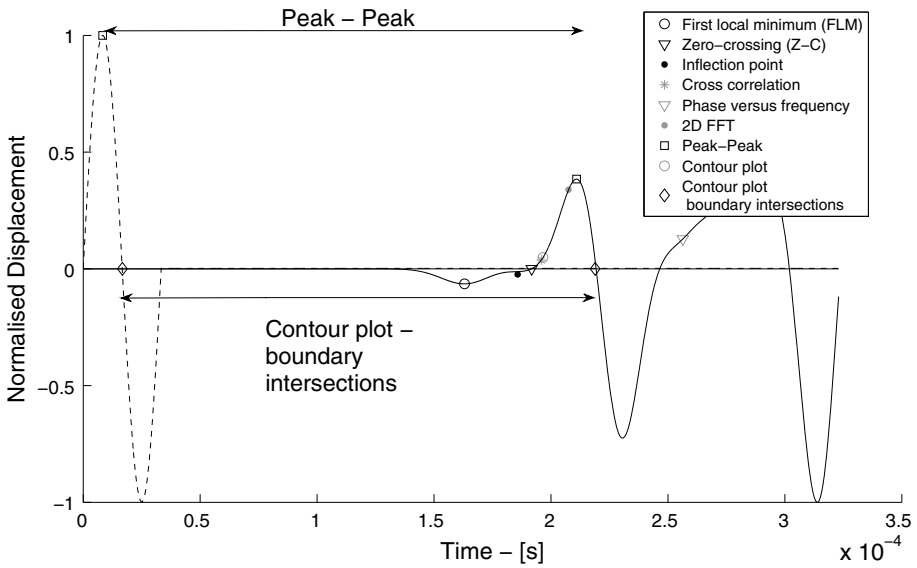

Fig. 4 Location of geometric characteristic arrival points on a typical received signal. $\sigma_0 = 100$ kPa, $f_{trans} = 30$ kHz, $R_d = 5.63$ and $\lambda/d_{50} = 6.40$. The dashed line indicates the transmitter displacement and the solid line indicates the observed receiver displacement. In both cases the displacements are normalised by the maximum values

poorly understood and will be explored with this simplified model.

Signal reflections at the boundary are known to influence received bender element signals and so it is important to establish the sensitivity of the observed response to the boundary conditions used. In a particle-scale analytical study Marketos and O'Sullivan [9] found that the lateral boundary conditions had a small, but measurable influence on the received signal. Using continuum modelling, Arroyo et al. [39] also found that boundary conditions had a small but measurable influence on their results. Here the sensitivity of the sample response to the boundaries was established by repeating the bender element simulation and using rigid walls to bound the sample along $y_{min} = 9.71 \times 10^{-3}$ mm and $y_{max} = 99.05$ mm and $z_{min} = 9.70 \times 10^{-3}$ mm and $z_{max} = 99.52$ mm. Also considered was the case where periodic boundaries bound the sample along $y_{min} = 10.01 \times 10^{-3}$ mm and $y_{max} = 99.05$ mm and $z_{min} = 9.69 \times 10^{-3}$ mm and $z_{max} = 99.52$ mm. As illustrated in Fig. 5, the amplitudes of the received signals differed in agreement with the data presented by Marketos and O'Sullivan [9]. The arrival time and frequency of oscillations of the initial disturbance were however, not noticeably affected by these changes to the boundaries.

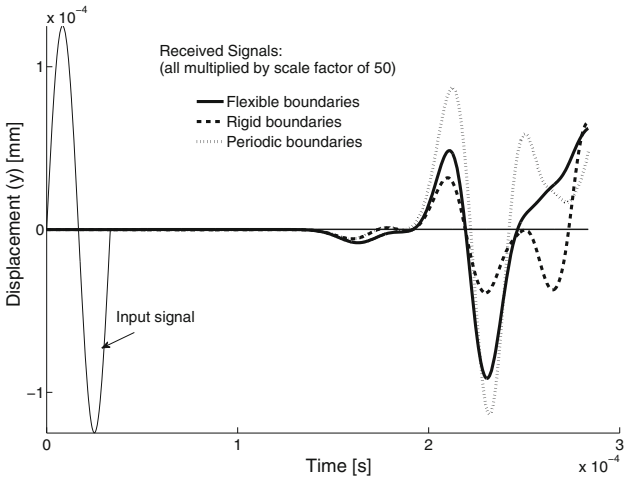

Fig. 5 Received signals (y-displacement) from the bender element tests on samples confined with flexible boundaries, rigid wall boundaries and periodic boundaries plotted against time. $\sigma_0 = 100$ kPa, $f_{trans} = 30$ kHz, $R_d = 5.63$ and $\lambda/d_{50} = 6.40$

When considering a dynamic response it is useful to review the system response by varying the transmitted frequency and observing the sensitivity to this variation. Clayton [6], amongst others, strongly advises the variation of the input frequency as a means to improve the reliability of the test results. The sensitivity of the received signal in the time domain to the input frequencies of 7, 15, 20 and 30 kHz is illustrated on Fig. 6. The received signal amplitude reduces as the transmitted frequency increases. The arrival of the main components of the waves occurs sooner as the transmitted frequency increases and this will be discussed more below after the travel time determination techniques are introduced.

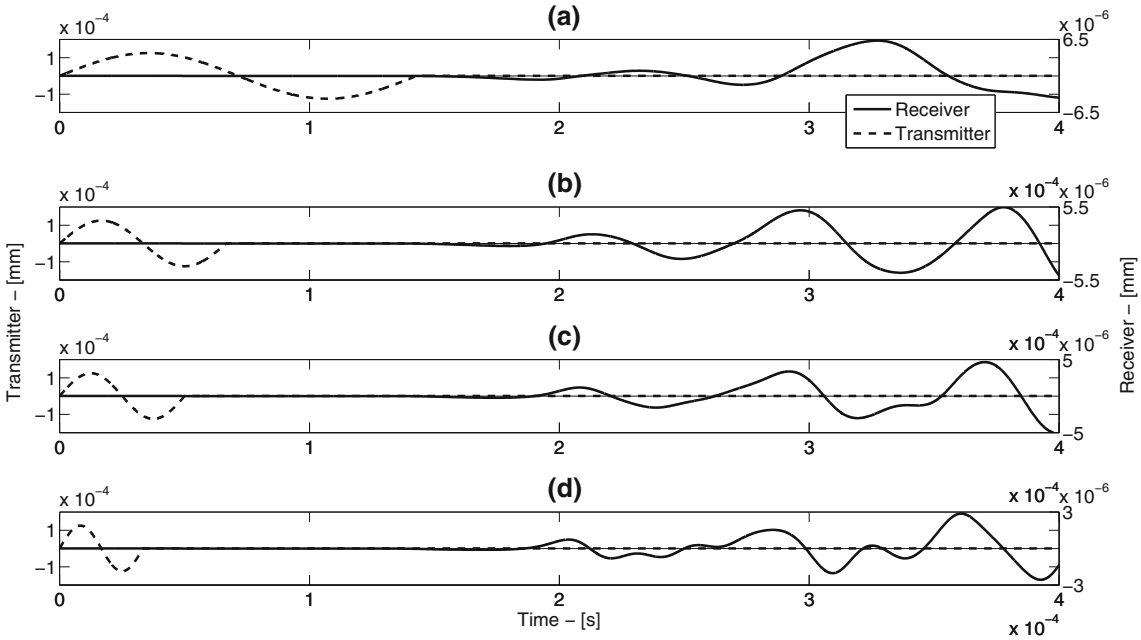

Fig. 6 Comparison of bender element transmitted signals (*dashed*) and bender element received signals (*solid*) transmitted with a single period sine pulse at different frequencies in the time domain **a** 7 kHz ($\sigma_0 = 100$ kPa, $R_d = 1.31$ and $\lambda/d_{50} = 27.4$), **b** 15 kHz ($\sigma_0 = 100$ kPa, $R_d = 2.81$ and $\lambda/d_{50} = 12.8$), **c** 20 kHz ($\sigma_0 = 100$ kPa, $R_d = 3.75$ and $\lambda/d_{50} = 9.60$), **d** 30 kHz ($\sigma_0 = 100$ kPa, $R_d = 5.63$ and $\lambda/d_{50} = 6.40$)

Table 2 G_{xy} values calculated using different travel time determination techniques for different transmitted frequency sine pulses

Sine pulses	G_{xy} [MPa] from different travel time determination techniques							
Frequency – [kHz]	Time domain interpretation of the received signal				Frequency domain interpretation of the received signal		Analysis of response of particles along line connecting receiver and transmitter	
	Peak–Peak	FLM	Infl. Pt.	Z-C	Phase	C–C	Contour plot	2D FFT
7	348	365	285	308	14	277	325	319
(ε^r)	(*9.3 %*)	(*14.6 %*)	(*−10.7 %*)	(*−3.4 %*)	(*−95.6 %*)	(*−13.2 %*)	(*1.9 %*)	(−)
15	347	414	298	354	51	342	367	319
(ε^r)	(*8.7 %*)	(*29.8 %*)	(*−6.6 %*)	(*11.0 %*)	(*−84.0 %*)	(*7.1 %*)	(*15.1 %*)	(−)
20	335	441	307	370	92	342	400	319
(ε^r)	(*5.0 %*)	(*38.3 %*)	(*−3.9 %*)	(*16.0 %*)	(*−71.0 %*)	(*7.1 %*)	(*25.3 %*)	(−)
30	350	459	325	388	204	349	347	311
(ε^r)	(*12.6 %*)	(*47.5 %*)	(*4.4 %*)	(*24.6 %*)	(*−34.4 %*)	(*12.3 %*)	(*11.4 %*)	(−)

ε^r is defined in Eq. 18

Table 3 Values of G_{xy} for the sample with the HM contact model calculated using the various travel time determination techniques at different confining pressures, 30 kHz input frequency

HM	G_{xy} – [MPa]							
	Time domain interpretation of the received signal				Frequency domain interpretation of the received signal		Analysis of response of particles along line connecting receiver and transmitter	
σ_0 – [kPa]	Peak–Peak	FLM	Infl. Pt.	Z-C	Phase	C–C	Contour plot	2D FFT
100	320	532	415	383	247	339	347	363
(ε^r)	(*−11.8 %*)	(*46.6 %*)	(*14.3 %*)	(*5.4 %*)	(*−31.9 %*)	(*−6.6 %*)	(*−4.5 %*)	(−)
200	401	659	517	505	100	431	446	445
(ε^r)	(*−9.9 %*)	(*47.9 %*)	(*16.2 %*)	(*13.4 %*)	(*−77.5 %*)	(*−3.2 %*)	(*0.1 %*)	(−)
300	455	739	592	568	184	492	512	504
(ε^r)	(*−9.6 %*)	(*46.7 %*)	(*17.5 %*)	(*12.7 %*)	(*−63.6 %*)	(*−2.4 %*)	(*1.6 %*)	(−)
500	588	859	701	663	162	585	593	592
(ε^r)	(*−0.7 %*)	(*45.2 %*)	(*18.5 %*)	(*12.1 %*)	(*−72.7 %*)	(*−1.2 %*)	(*0.3 %*)	(−)
750	672	966	786	750	162	671	687	670
(ε^r)	(*0.4 %*)	(*44.1 %*)	(*17.3 %*)	(*11.9 %*)	(*−75.8 %*)	(*0.1 %*)	(*2.53 %*)	(−)
1000	848	1005	859	892	298.70	778	765	714
(ε^r)	(*18.7 %*)	(*40.8 %*)	(*20.31 %*)	(*25.0 %*)	(*−58.2 %*)	(*9.0 %*)	(*7.1 %*)	(−)

ε^r is defined in Eq. 18

There is significant uncertainty and difficulty associated with determining the travel time in bender element tests by methods that rely on analysis of the received signal (e.g. [2,4,34,37]). When interpreting the received signal in the time domain, it is typical to consider either the peak-peak time or the first break/first arrival methods (e.g. [6,40]). The peak–peak method takes the time between the first peak in the input signal and the first peak in the received signal; Clayton [6] argues that it is easier to pick consistent peak-peak travel times in comparison with first arrival times and the objectivity of this measure is clearly illustrated in Fig. 4. Selecting the first arrival method is less straightforward. Referring to what they describe as a typical test Ferreira and da Fonseca [40] say that there is an error margin of 20 % in identifying this point, and da Fonseca et al. [5] show that there is subjectivity associated with identifying the exact arrival point. Here, the absence of high frequency noise that is typical of a laboratory signal enabled three objective arrival points to be identified. These are:

(i) The first local minimum point (FLM on Fig. 4);
(ii) The point where the received signal crosses the horizontal axis, i.e. the zero-crossing point (Z-C on Fig. 4);
(iii) The point of inflection, this mathematically is the second point on the received signal where the second derivative is zero (Infl. Pt on Fig. 4).

Table 4 Values of G_{xy} for the sample with the HMD contact model calculated using the various travel time determination techniques at different confining pressures

HMD	G_{xy} – [MPa]							
	Time domain interpretation of the received signal				Frequency domain interpretation of the received signal		Analysis of response of particles along line connecting receiver and transmitter	
σ_0 – [kPa]	Peak–Peak	FLM	Infl. Pt.	Z-C	Phase	C–C	Contour plot	2D FFT
100	219	299	300	247	106	265	296	293
(ε^r)	(−25.4 %)	(2.1 %)	(2.6 %)	(−15.7 %)	(−63.9 %)	(−9.5 %)	(1.1 %)	(−)
200	271	370	372	305	107	321	362	358
(ε^r)	(−24.4 %)	(3.4 %)	(3.9 %)	(−14.9 %)	(−70.2 %)	(−10.4 %)	(1.2 %)	(−)
300	325	413	412	340	107	338	432	422
(ε^r)	(−22.8 %)	(−2.2 %)	(−2.4 %)	(−19.4 %)	(−74.7 %)	(−20.0 %)	(2.4 %)	(−)
500	376	485	486	391	108	362	506	506
(ε^r)	(−25.7 %)	(−4.1 %)	(−4.0 %)	(−22.7 %)	(−78.6 %)	(−28.4 %)	(0.0 %)	(−)
750	428	547	548	444	109	534	557	566
(ε^r)	(−24.4 %)	(−3.3 %)	(−3.2 %)	(−21.7 %)	(−80.8 %)	(−5.7 %)	(−1.7 %)	(−)
1000	461	597	597	489	107	591	640	602
(ε^r)	(−23.4 %)	(−0.9 %)	(−0.9 %)	(−18.8 %)	(−82.2 %)	(−1.9 %)	(6.2 %)	(−)

ε^r is defined in Eq. 18

Table 5 Values of G_{xy} for the sample with the CM contact model calculated using various travel time determination techniques at different confining pressures

CM	G_{xy} – [MPa]							
	Time domain interpretation of the received signal				Frequency domain interpretation of the received signal		Analysis of response of particles along line connecting receiver and transmitter	
σ_0 – [kPa]	Peak–Peak	FLM	Infl. Pt.	Z-C	Phase	C–C	Contour plot	2D FFT
100	139	312	180.07	163.67	88.15	135.44	218	178
(ε^r)	(−22.4 %)	(75.1 %)	(0.9 %)	(−8.3 %)	(−50.6 %)	(−24.1 %)	(22.2 %)	(−)
200	193	514	284	223	83	151	332	267
(ε^r)	(−27.8 %)	(92.3 %)	(6.3 %)	(−16.7 %)	(−69.1 %)	(−43.6 %)	(24.3 %)	(−)
300	216	581	321	257	105	167	316	326
(ε^r)	(−33.8 %)	(78.1 %)	(−1.4 %)	(−21.0 %)	(−67.8 %)	(−48.7 %)	(−3.2 %)	(−)
500	260	721	366	264	106	241	352	374
(ε^r)	(−30.4 %)	(93.0 %)	(−2.1 %)	(−29.5 %)	(−71.8 %)	(−35.4 %)	(−5.7 %)	(−)
750	282	673	418	378	106	265	378	421
(ε^r)	(−33.1 %)	(59.9 %)	(−0.6 %)	(−10.3 %)	(−74.8 %)	(−37.0 %)	(−10.3 %)	(−)
1000	310	701	471	464	106	290	395	472
(ε^r)	(−34.4 %)	(48.6 %)	(−0.2 %)	(−1.8 %)	(−77.6 %)	(−38.5 %)	(−16.3 %)	(−)

ε^r is defined in Eq. 18

Tables 2, 3, 4 and 5 list the resulting shear stiffness values for the range of simulations considered in this study assuming a sample density value, $\rho = 1600\,\text{kg/m}^3$. The data in Table 2 considers the sensitivity of the measured stiffness values to the frequency of the input signal. Referring to Fig. 6, the point at which the received signal crossed the horizontal axis following the initial deflection (first zero crossing point) is clearly sensitive to the input frequency. Thus it is perhaps not surprising that the calculated stiffness using these four arrival time-based methods vary with frequency, as indicated on Table 2. Table 3 considers the simplified Hertz–Mindlin contact model for various confining

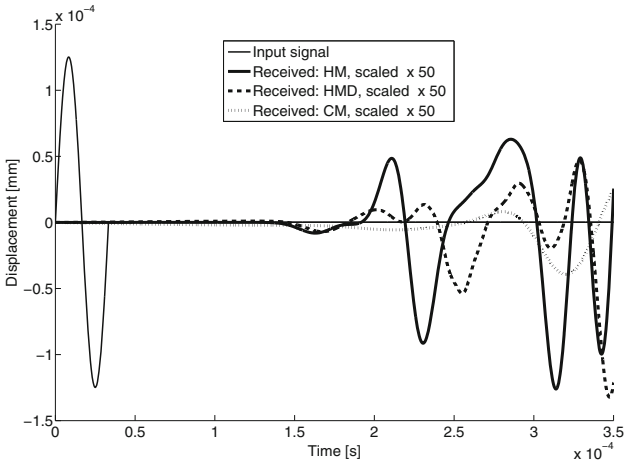

Fig. 7 Received signals (y-displacement) from the bender element tests on samples with the HM contact model, CM contact model and HMD contact model plotted against time. HM: $\sigma_0 = 100\,\text{kPa}$, $f_{trans} = 30\,\text{kHz}$, $R_d = 5.63$ and $\lambda/d_{50} = 6.40$, CM: $\sigma_0 = 100\,\text{kPa}$, $f_{trans} = 30\,\text{kHz}$, $R_d = 8.22$ and $\lambda/d_{50} = 4.38$, HMD: $\sigma_0 = 100\,\text{kPa}$, $f_{trans} = 30\,\text{kHz}$, $R_d = 6.41$ and $\lambda/d_{50} = 5.62$

pressures. Tables 4 and 5 consider the data for the simulation using the Hertz–Mindlin–Deresiewicz and Cavarretta–Mindlin contact model respectively; representative receiver signals for these models are included as Fig. 7. The data presented in Tables 3, 4 and 5 and the general trends observed, will be discussed in more detail later, however they are introduced at this juncture to further highlight the large differences that can exist in the results obtained using these four arrival time approaches. It is clear that there is poor agreement amongst the four geometric point methods, and the sensitivity of all of the methods to the frequency input indicates a general lack of robustness. The current three-dimensional study therefore confirms results obtained with the more simplified semi-analytical two-dimensional study [9].

4 Particle-scale response in time domain

Both the temporal and spatial variation in the response of the entire system can be appreciated via the series of twelve discrete "snapshots" at intervals of half the input wave period (i.e. at intervals of 1.67×10^{-5} s) presented in Figs. 8 and 9. In all cases a sectional plan view of the sample response in the plane of the transmitter and receiver elements is illustrated (xy-plane). The particle translational velocities are plotted as vectors with orientations and magnitudes indicated by the x- and y-components of the translational velocities. For clarity velocities exceeding 0.5 mm/s (that occur close to the transmitter particle) are omitted. The system response is clearly complex and differs from the assumption of plane wave transmission between transducers that is the basis for test interpretation, as outlined by Arroyo et al. [39]. A circular s-wave lobe centred on the transmitter propagates towards the receiver, while two, oppositely polarized p-wave lobes move from the transmitter radially outwards towards the boundaries. This was anticipated by Lee and Santamarina [37] from their experimental work on wave propagation. The magnitude of the velocities reduces as the shear wave moves through the system, indicating reduction in amplitude due to geometric spreading. Initially (at points *a*–*e*) the plot of velocity vectors is not symmetric. By point *f* there appears to be a series of almost circular wave fronts moving through the sample, but it is not clear which the most significant wave front is. Reflections are evident by time point *f*. Movement is recorded at the receiver between time points *i* and *j*, i.e. before arrival of the main shear wave front. The shear wave arrives at the received signal at some time between points *k* and *l* (the receiver particle is a particle diameter inside the boundary). Memory considerations limited output of the data for each particle to discrete time increments, and while the arrival of the shear wave is close to the inflection and zero-crossing points, the shear wave arrival cannot precisely be associated with one of the characteristic points identified on Fig. 4 with this level of temporal discretization.

By considering the y-displacement of a column of particles along a straight line from the transmitter to the receiver the three dimensional plot illustrated in Fig. 10 was created. This gives displacement as a function of position and time for an input frequency of 30 kHz. In this plot the initial wave front is clearly distinguishable and it is also clear that at later times the system response is strongly influenced by the boundary reflections. The data presented in Fig. 10 is more quantitatively interpreted using a two-dimensional contour plot of particle displacements. Figure 11 shows a distinct contour line emerging from the transmitter (position = 0) at a time of 3.33×10^{-5} s, i.e. midway through the input disturbance. The average slope of this line (479 m/s) can be taken as the shear wave velocity, V_{xy}. It is difficult to associate the beginning and end of a given contour with a particular characteristic point on the receiver signal as there are a large number of almost parallel contour lines. However, on Fig. 4 the start and end points of the contour line originating from the middle of the transmitted signal are indicated. The shear stiffness values obtained using these contour plot approaches are included in Tables 2, 3, 4 and 5. The steeper contours which precede the contour originating at the centre of the transmitted signal are associated with the near-field effect. This near-field effect is the result of faster moving compressional waves produced by the transmitter that propagate through the system and arrive at the receiver before the shear wave [38].

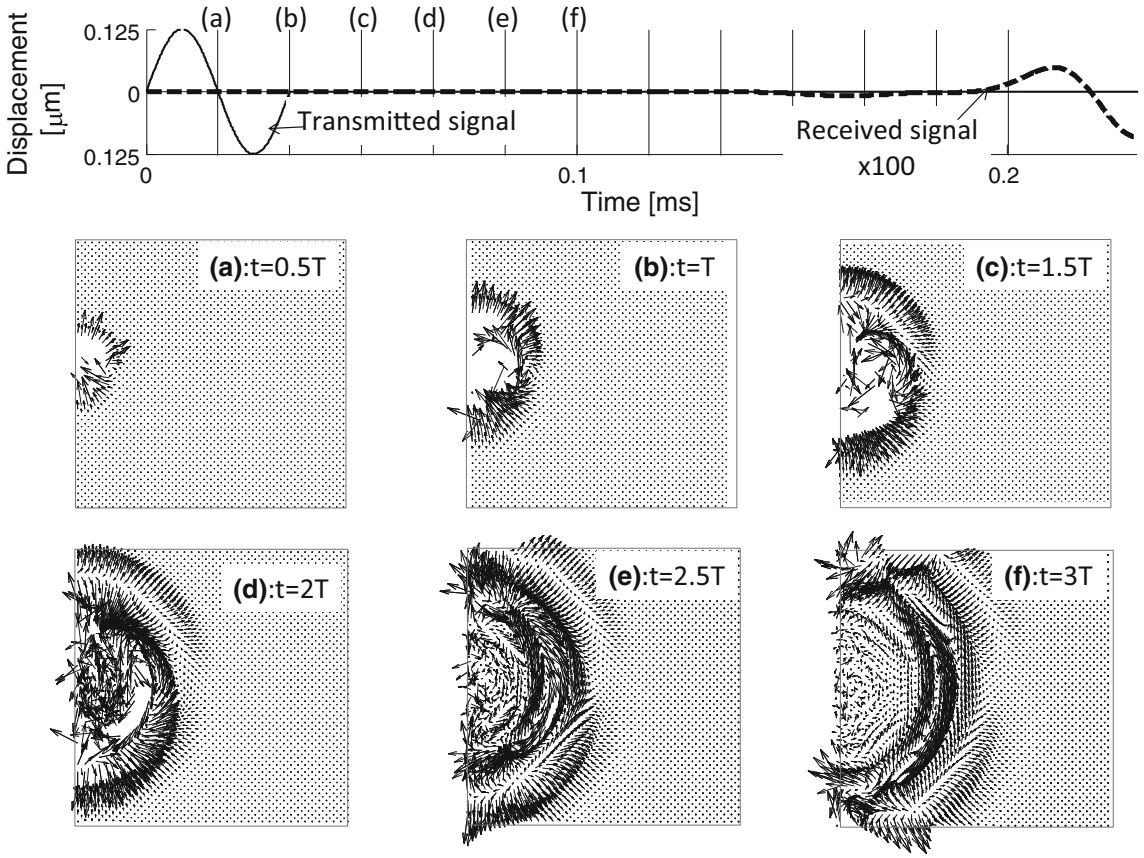

Fig. 8 Individual particle velocity vectors produced by a bender element test (x and y components) scaled by magnitude considering x and y components of velocity only. View is a plan view of a 5 mm thick cross-section through the sample. Only particle velocities $\leq$0.5 mm/s magnitude are plotted to prevent larger velocities from "clouding" the system response. Time points **a**–**f** are shown in this plot. $\sigma_0 = 100$ kPa, $f_{trans} = 30$ kHz, $R_d = 5.63$ and $\lambda/d_{50} = 6.40$

5 System response in frequency domain

Figure 12 presents plots of amplitude versus frequency obtained by applying a fast Fourier transform (FFT) to both the input and recorded signals for frequencies between 7 and 30 kHz. It is clear in all cases that a single sine pulse is a complex wave form, containing a range of frequencies, with the maximum transmitted frequency being approximately twice the nominal frequency. The range of frequencies in the received signals is similar. It is interesting to note that there are distinct peaks in the received signal data, this type of local maxima are also evident in the frequency domain data presented by Alvarado and Coop [1] and Arroyo et al. [39]. Considering the sample as a linear system following [1] and [9] the sample is considered as having multiple natural modes of vibration. The range of frequencies present in the input signal overlaps with the range of natural frequencies for the granular sample as is calculated by approaches similar to [9]; thus these natural frequencies are excited by the input signal.

As well as the sensitivity to the input frequency, the dynamic response of the system varies when the system stiffness varies. Where the Hertz–Mindlin contact model is used, the system stiffness varies with confining pressure in the absence of any change in void ratio, such that $G \propto {\sigma_0'}^{1/3}$ (e.g. [41]). Figure 13 compares the received signal responses observed for a range of sample confining pressures between 100 kPa and 1 MPa in the frequency domain for the same input displacement of the receiver. As the confining pressure increased, the number of peaks in the received signal reduced.

An impression of the variation in the observed frequency domain response of the sample as the wave propagated through the sample was obtained by repeatedly determining the FFTs of the particle displacement data for a column of particles joining the transmitter and receiver particles. Considering the case of an input frequency of 30 kHz and a confining pressure of 100 kPa, the resultant data are plotted on Fig. 14 where the shading indicates amplitude in metres. Figure 14 clearly indicates that there is a marked decrease in the amplitudes of the higher frequency components of motion as the wave passes through the sample (i.e. with increasing distance from the transmitter). The data show that the sample acts as a filter, removing the higher frequency modes as

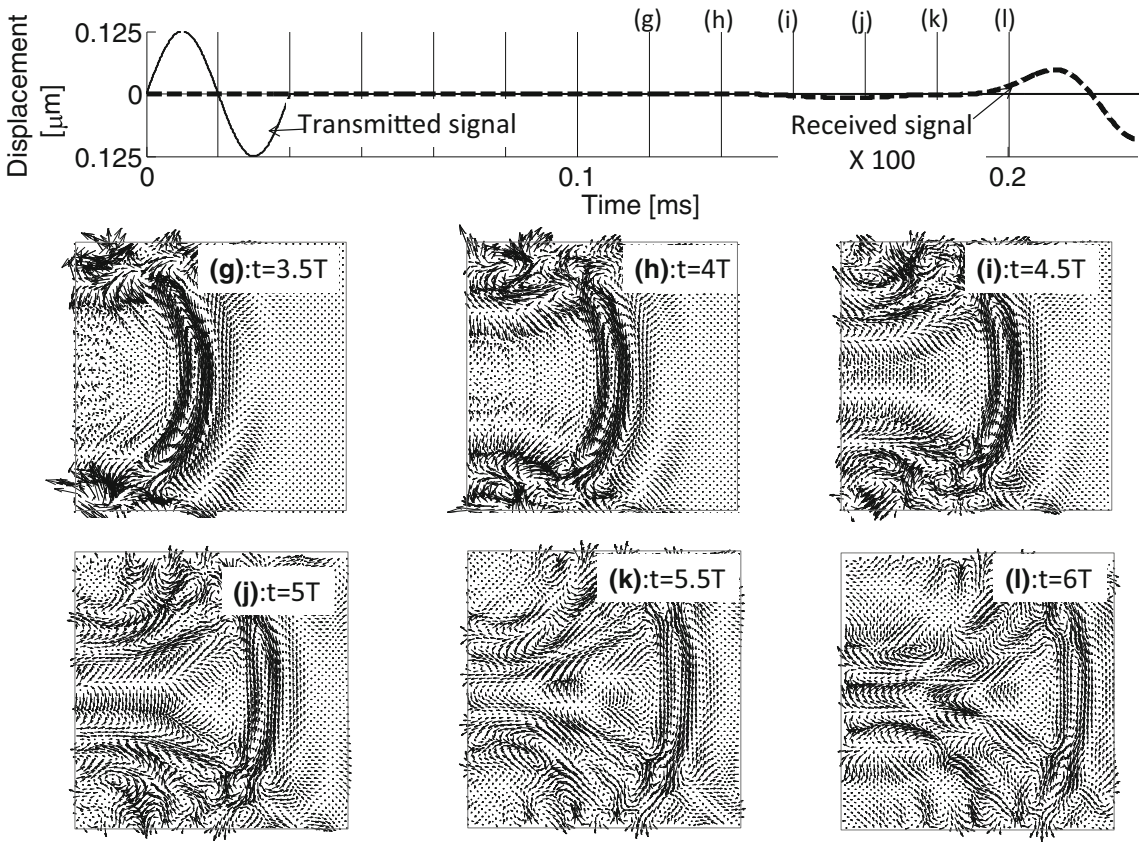

Fig. 9 Individual particle velocity vectors produced by a bender element test (x and y components) scaled by magnitude considering x and y components of velocity only. View is a plan view of a 5 mm thick cross-section through the sample. Only particle velocities ≤0.5 mm/s magnitude are plotted to prevent larger velocities from "clouding" the system response. Time points **g–l** are shown in this plot. $\sigma_0 = 100\,\text{kPa}$, $f_{trans} = 30\,\text{kHz}$, $R_d = 5.63$ and $\lambda/d_{50} = 6.40$

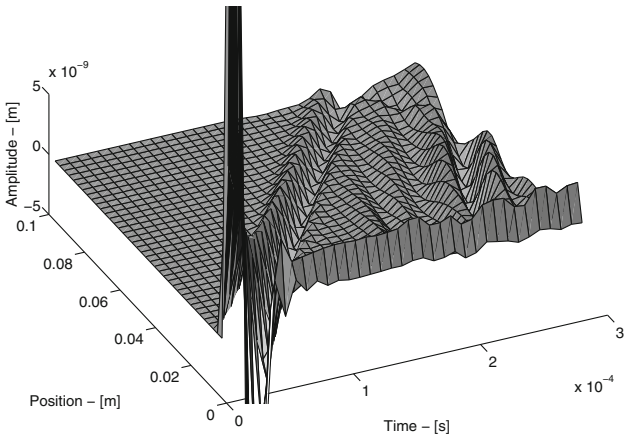

Fig. 10 Time-domain surface plot of position versus time where the peaks are measured by the displacement in the y-direction. This shear wave was produced by a bender element test. $\sigma_0 = 100\,\text{kPa}$, $f_{trans} = 30\,\text{kHz}$, $R_d = 5.63$ and $\lambda/d_{50} = 6.40$

the signal propagates through the sample as was observed by [14].

The raw output from the FFT takes the form of a series of complex numbers, and the phase angles (φ) of these complex numbers can be plotted against their associated frequencies, as illustrated in Fig. 15 (input signal 30 kHz). The secant slope to this line at a given frequency, f, gives the wave travel time associated with that frequency $\left(t_{arr} = \frac{\varphi}{2\pi f}\right)$ and hence the phase velocity, while the tangent slope gives the group velocity [42]. The velocities measured using this method were lower than all other methods as is shown below. It was recommended by da Fonseca et al. [5] and Greening and Nash [42] that a continuous signal be used as the transmitted signal to improve reliability. In this research an input signal that was a sine pulse repeated ten times did not improve the reliability of this method. In line with the prior observations of Lawney and Luding [43] who considered a one-dimensional system analytically and Alvarado and Coop [1] who considered experimental data the phase and group velocities differ. This means that the system is dispersive. The fact that different wave components will travel at different speeds will therefore affect the reliability of picking characteristic points on the received signal and using these so as to calculate a sample stiffness value. The shape of the wave signal will also change as this propagates through the sample (see also Marketos and O'Sullivan [9]).

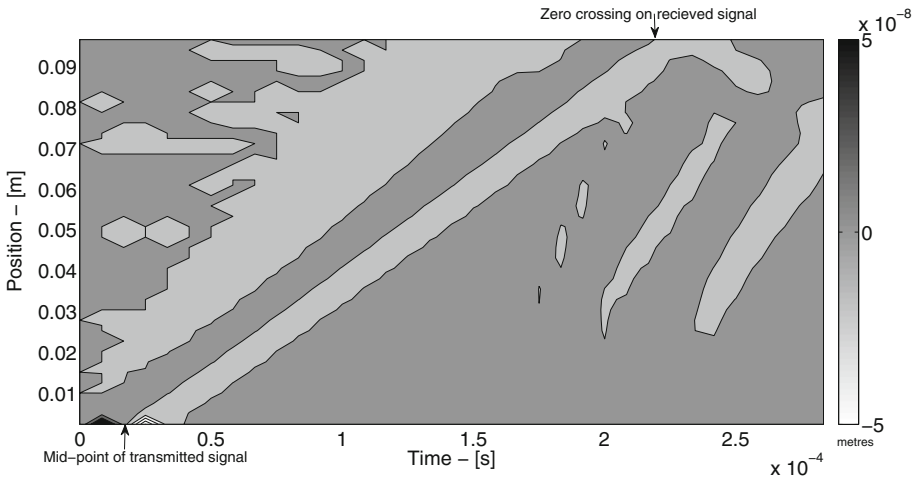

Fig. 11 Time-domain contour plot of position versus time where the contours are coloured by the displacement in the y-direction. This shear wave was produced by a bender element test. $\sigma_0 = 100\,\text{kPa}$, $f_{trans} = 30\,\text{kHz}$, $R_d = 5.63$ and $\lambda/d_{50} = 6.40$

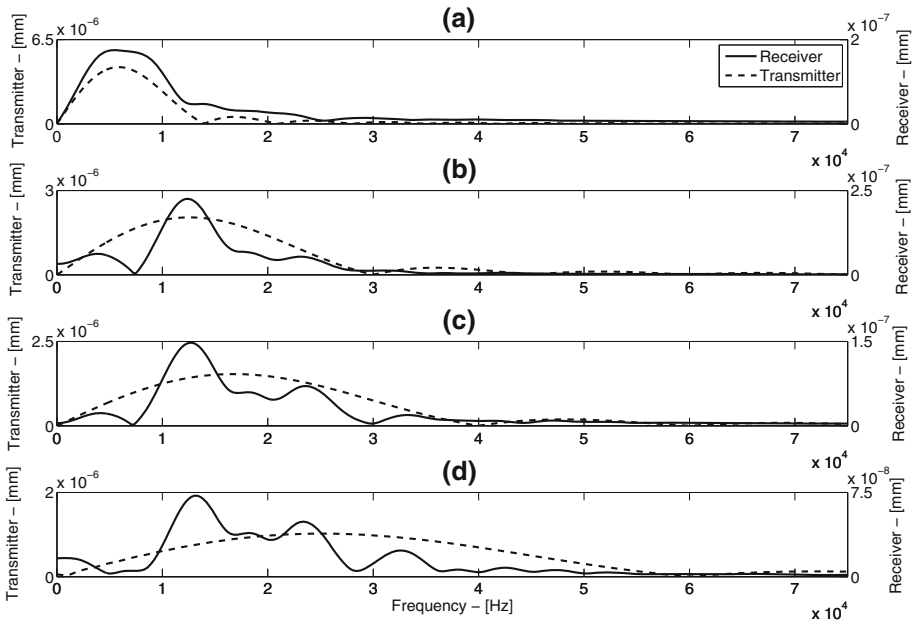

Fig. 12 Comparison of normalised transmitted signals (*dashed*) and normalised received signals (*solid*) produced by a bender element test transmitted with a single period sine pulse at different frequencies in the frequency domain **a** 7 kHz ($\sigma_0 = 100\,\text{kPa}$, $R_d = 1.31$ and $\lambda/d_{50} = 27.4$), **b** 15 kHz ($\sigma_0 = 100\,\text{kPa}$, $R_d = 2.81$ and $\lambda/d_{50} = 12.8$), **c** 20 kHz ($\sigma_0 = 100\,\text{kPa}$, $R_d = 3.75$ and $\lambda/d_{50} = 9.60$), **d** 30 kHz ($\sigma_0 = 100\,\text{kPa}$, $R_d = 5.63$ and $\lambda/d_{50} = 6.40$)

Following the approach of Mouraille et al. [14] and de Mol [44], a two-dimensional FFT can be applied to the particles connecting the transmitter and receiver to generate a plot of angular velocity ($\omega = 2\pi f$) versus wavenumber ($k = 2\,\pi\,/\lambda$), as illustrated in Fig. 16. The spectral amplitude at a given combination of ω and k is indicated using shading. There is a distinguishable region of maximum spectral amplitude with a quantifiable slope in $\omega - k$ space and the slope of this line (obtained via a linear least squares regression) gives an estimate of wave speed, in this case a value of 471 m/s was obtained. This method is termed the two-dimensional fast Fourier method (2D FFT method). Figure 16 shows that there is a region of the sample for which the frequency of the dominant component of the wave is proportional to the wavenumber and this does not imply the system is not dispersive. Rather, Fig. 16 indicates that most of the energy of the wave travels through the middle of the system with a certain velocity that can be calculated from the slope of the shaded region. The high frequencies present in the input signal seem to be trapped close to the transmitter edge of the sample. The dispersive nature of the system is confirmed by the fact that the shape of the wave changes markedly as it passes through the sample (note though the signal shape is also affected by reflections off boundaries). The stiffness values obtained using this method are also indicated on Tables 2, 3, 4 and 5. Referring to Table 2, it is clear that this method is less sensitive to the frequency of the input signal than any of the other methods.

6 Reliability of stiffness measurement

The regular, lattice nature of the packing enables both analytical determination of the stiffness, as well as use of stress

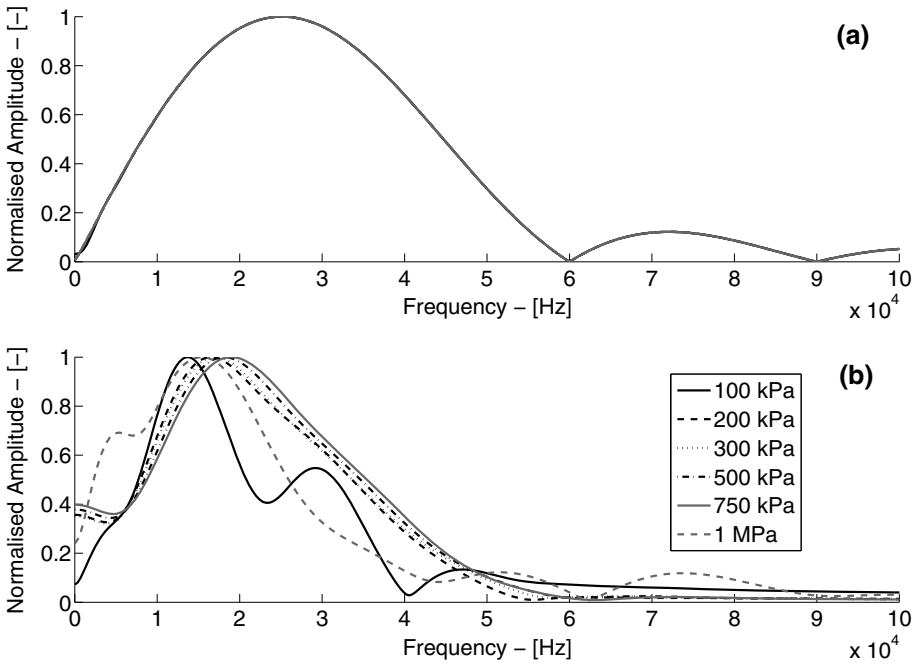

Fig. 13 Normalised amplitude versus frequency for different confining pressures. The shear waves were produced by a bender element test. **a** Transmitted sine pulses, **b** received sine pulses. ($\sigma_0 = 100$ kPa, $f_{trans} = 30$ kHz, $R_d = 5.63$ and $\lambda/d_{50} = 6.40$; $\sigma_0 = 200$ kPa, $f_{trans} = 30$ kHz, $R_d = 5.01$ and $\lambda/d_{50} = 7.18$; $\sigma_0 = 300$ kPa, $f_{trans} = 30$ kHz, $R_d = 4.69$ and $\lambda/d_{50} = 7.68$; $\sigma_0 = 500$ kPa, $f_{trans} = 30$ kHz, $R_d = 4.30$ and $\lambda/d_{50} = 8.37$; $\sigma_0 = 750$ kPa, $f_{trans} = 30$ kHz, $R_d = 4.02$ and $\lambda/d_{50} = 8.95$; $\sigma_0 = 1$ MPa, $f_{trans} = 30$ kHz, $R_d = 3.83$ and $\lambda/d_{50} = 9.39$)

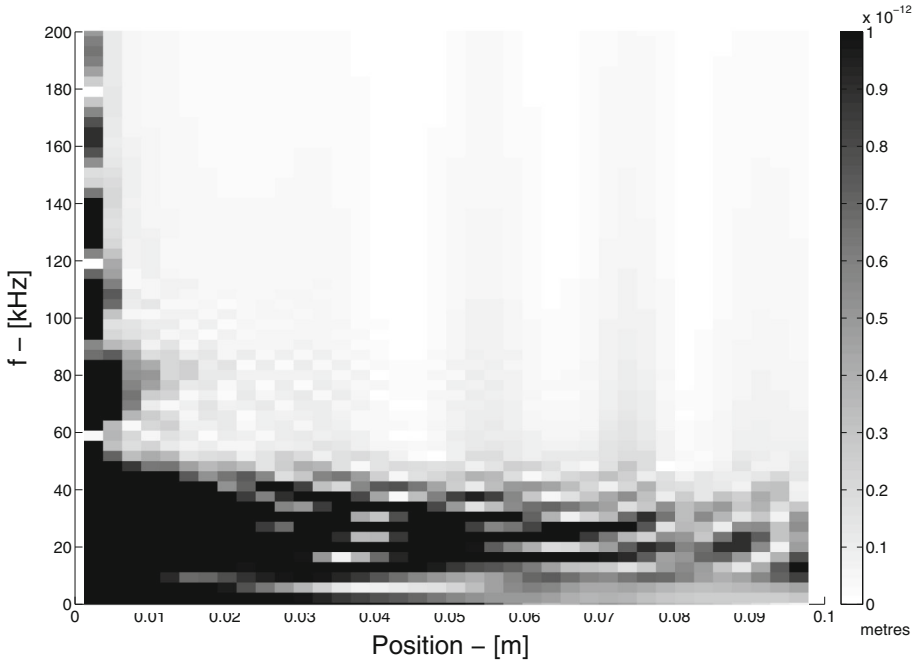

Fig. 14 Plot of frequency versus position coloured by amplitude. The shear wave was produced by a bender element test. *Black* indicates higher amplitude values than *white*. $\sigma_0 = 100$ kPa, $f_{trans} = 30$ kHz, $R_d = 5.63$ and $\lambda/d_{50} = 6.40$

probes to give independent measures of stiffness. Prior published comparisons between analytically-derived estimates of stiffness and DEM simulations of quasi-static stress probes include [45] and [46]. The analytical estimates presented here were obtained using effective medium theory (EMT), a principle of virtual displacement approach (PVD) and dispersion relation theory (DRT).

Figure 17 plots the results from stress probes carried out on the system to calculate G_{xy}, the regular packing considered here means that these are constant fabric stress probes and should give results equivalent to those obtained in wave propagation [47]. Two measurement regions were used namely the whole sample and the measurement sphere which was a spherical region situated in the centre of the sample and had a diameter that was 80 % of the sample length. Representative particle stresses were measured and homogenised to a sample stress tensor using the method outlined by Itasca Consulting Group [23] and Cundall and Strack [25] that uses a volume-based averaging technique. The best-fit method of measuring a particle based sample strain tensor, out-

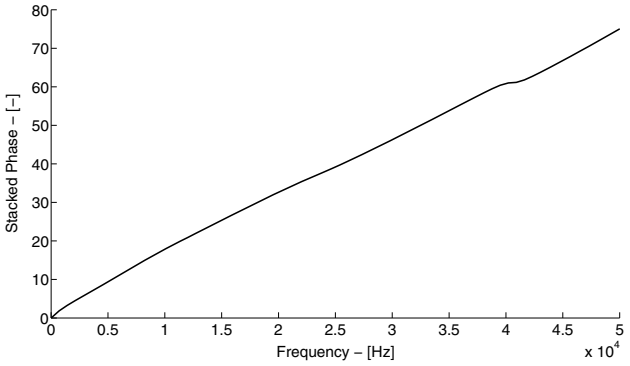

Fig. 15 Stacked phase versus frequency. The shear wave produced by a bender element test. $\sigma_0 = 100\,\text{kPa}$, $f_{trans} = 30\,\text{kHz}$, $R_d = 5.63$ and $\lambda/d_{50} = 6.40$

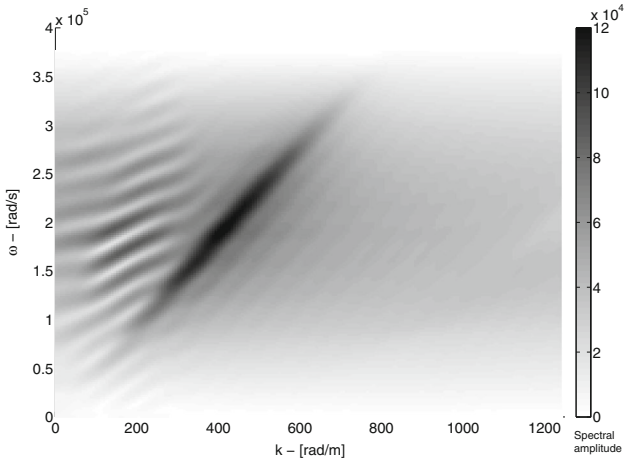

Fig. 16 Plot of angular velocity versus wavenumber (inverse of the wavelength) coloured by the magnitude of the y-velocity. The shear wave was produced by a bender element test. *Black* indicates higher wave energy than *white*. $\sigma_0 = 100\,\text{kPa}$, $f_{trans} = 30\,\text{kHz}$, $R_d = 5.63$ and $\lambda/d_{50} = 6.40$

lined in [48] and [49] was used. As the sample was cubic-anisotropic the following equation was used to calculate the value of G_{xy}

$$G_{xy} = \frac{E_z}{2(1+\nu_{zx})} \tag{15}$$

where E_z is the Young's modulus in the vertical direction and ν_{zx} is the Poisson's ratio in the zx-plane. E_z was calculated from a best-fit of the axial stress versus axial strain and ν_{zx} was calculated from a best-fit of the transverse strain versus axial strain. The above equation was derived by Lings [50]. Norris [51] is an example of where equations governing the directional dependence of parameters can be found. Equation 15 was used as the waves were propagating and oscillating at 45° to the principal directions of the packing.

The G_{xy} values obtained using the 2D FFT method are included with the stress probe data on Fig. 17. The maximum percentage error between G_{xy} values measured using stress probes and G_{xy} values measured using wave propagation tests (2D FFT) was approximately 10 %, i.e. less than the difference between many of the previously proposed laboratory interpretation methods (Tables 2, 3, 4 and 5). It is important to consider both the values of G_{xy} at a given σ_0 and the slopes of the lines which are also listed.

EMT is an approach where the overall properties of the material are estimated by averaging over the discrete elements of the material and it was used to develop estimates of stiffness of granular media by a number of researchers [21,52]. Santamarina and Cascante provide the following expressions for effective medium theory shear stiffness (G^{EMT}) and an effective medium theory Poisson's ratio (ν^{EMT}):

$$G^{EMT} = \frac{(4-3\nu)\left[\frac{3\sigma_0 G_{part}^2}{2(1-\nu_{part})^2}\right]^{1/3}}{2\left(2-\nu_{part}\right)} \tag{16}$$

$$\nu^{EMT} = \frac{\nu_{part}}{8-5\nu_{part}} \tag{17}$$

where G_{part} and ν_{part} are the shear stiffness and Poisson's ratio of the solid material making up the particles. The expression for G^{EMT} does not consider packing anisotropy and, given that the material considered is cubic anisotropic, it can be expected that G^{EMT} will only be an approximate value.

Mouraille et al. [14] and de Mol [44] used a principle of virtual displacement approach (PVD) to derive an expression for the 4th order stiffness tensor ($C_{\alpha\beta\gamma\phi}$) that relates the stress ($\sigma_{\alpha\beta}$) and strain ($\varepsilon_{\gamma\phi}$) tensors by $\delta\sigma_{\alpha\beta} = C_{\alpha\beta\gamma\phi}\delta\varepsilon_{\gamma\phi}$. The potential energy at the contact is calculated by considering the strain energy at the contact. The first derivative of the potential energy density with respect to the second order strain tensor gives a second order stress tensor and the derivative of the second order stress tensor with respect to strain gives a fourth order stiffness tensor.

A second analytical approach considered by De Mol [44] and Mouraille [53] is based on dispersion relation theory (DRT). In this approach a unit cell in the lattice is considered, with the particle-based stiffness tensor (S) and mass tensor (M). The harmonic wave equation is used to establish the displacement at the contact when a wave propagates through the system. A compatibility parameter (D) relates the wave equation to the overlap produced. Adopting the notation used by Mouraille and de Mol the resulting eigenvalue problem is $[K - \omega^2 M]U = 0$, (where K equals the product of S and D) with a solution equal to U_0. K represents the relationship between the displacement at the contact predicted by the harmonic wave equation and the contact force acting on each particle. U_0 represents the eigenmodes and these eigenmodes are associated with rotational and transverse motion, with some modes representing coupled shear-rotational motion as highlighted by Merkel et al. [54] and [55]. The wavenumber vector (k) is used to establish the direction and plane of

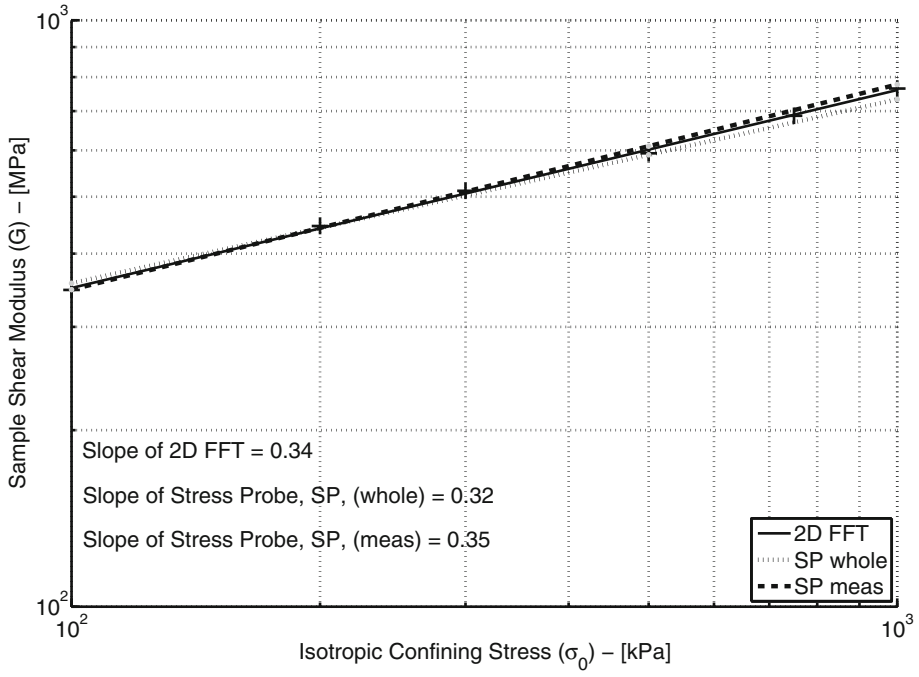

Fig. 17 Results from stress probes carried out on the sample confined at 100, 500 kPa and 1MPa are compared with the results from wave propagation tests—measured using the 2D FFT method. Two measurement regions were used to record stress and strain values in the stress probe tests: the whole sample and the measurement sphere

propagation. For example, a wavenumber $k = [0;\ 0;\ k]$, produces a compressional wave travelling in the z-direction and the associated shear waves propagating in the z-direction and oscillating in the x- or y-directions. A plot of angular velocity versus wave number gives the wave velocity for a given wave, from which the stiffness G^{DRT} can be derived.

The estimates of G obtained using the analytical methods presented above are illustrated in Fig. 18. The Santamarina and Cascante expression (Eqs. 16, 17) indicates that $G \propto \sigma_0^{1/3}$ (i.e. $\alpha = 1/3$). These expressions do not consider orientation or direction. The principle of virtual displacement and dispersion relation theories give values of G that depend on the direction orientation. The xy-plane was used to compare with the wave propagation results. All the α values are similar and are close to 1/3. The wave propagation results measured using the 2D FFT method agrees well with the G_{xy} results from the principle of virtual displacement and the G_{xy} results from effective medium theory although the analytical methods do overestimate the stiffness. The dispersion relation G values are not as close in magnitude to the results measured using the 2D FFT method. It appears that this method tends to overestimate stiffness more than the other analytical methods.

7 Reliability of stiffness measurement: comparison of available approaches

The good comparison with the stress probes and a number of the analytical methods confirmed that the 2D FFT method is useful to interpret wave propagation tests and including bender element tests, provided measurements of the signal are made at multiple sampling points. The validity of the 2D FFT method is also supported by the particle-scale data on Figs. 8 and 9 where arrival appears to occur around time point l resulting in a shear wave speed that closely matches the resulting shear wave speed from the 2D FFT method. The lack of sensitivity of the calculated shear stiffness values to the frequency of the input signal further confirms the robustness of this wave-based approach. Obviously the 2D FFT method is of limited use in a conventional laboratory bender element test; however, it can be used as a benchmark against which methods that can be used in the laboratory can be tested. Tables 2, 3, 4 and 5 list the percentage errors, ε^r for the G_{xy} values calculated using all of the other interpretative methods, relative to the 2D FFT method:

$$\varepsilon^r = \frac{G_{xy}^m - G_{xy}^{2DFFT}}{G_{xy}^{2DFFT}} \times 100 \tag{18}$$

where G_{xy}^m is the G_{xy} calculated using particular method m.

Table 2 summarises the results from a parametric study varying the simulated transmitted frequency. With the exception of the 2D FFT method, all the travel time determination methods gave G_{xy} values that increased with transmitted frequency. This suggests that these methods are not accurately capturing the material response as the measured G_{xy} should be independent of transmitter frequency. There is good agreement between the 2D DEM interpretation techniques of displacement contours (Fig. 11) and the data generated using the 2D FFT (Fig. 16). Ferreira and da Fonseca [40] note that varying the frequency and shape of the input wave can

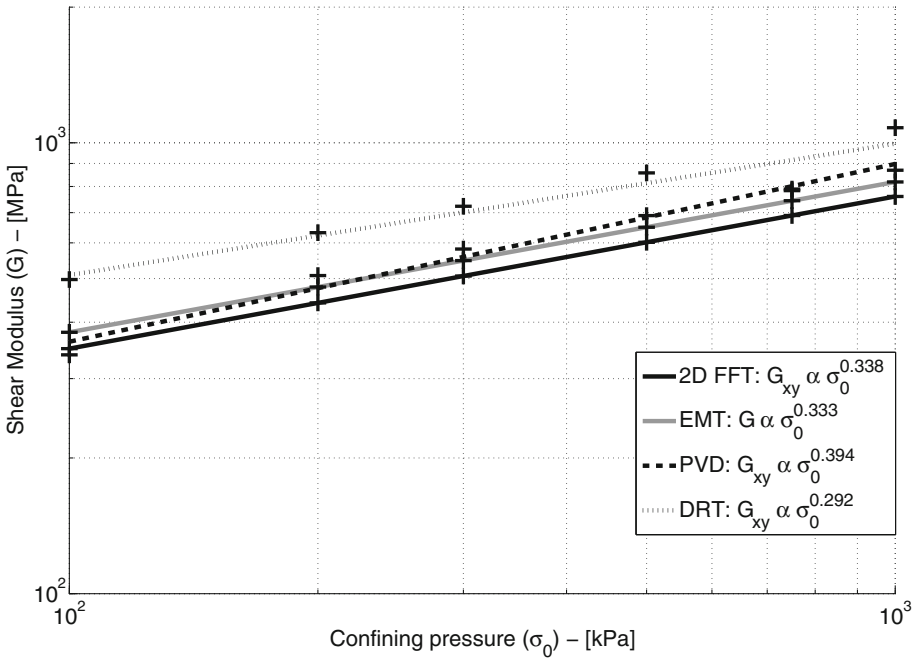

Fig. 18 Calculated values of shear modulus in the xy-plane (G_{xy}) for different confining pressures using different analytical methods. *EMT* effective medium theory, *PVD* principle of virtual displacement, *DRT* dispersion relation theory and *2D FFT* two-dimensional fast Fourier transform

improve confidence in picking the first arrival point. All of the geometric point methods considered here give an arrival time that decreases with increasing frequency. The point of first local minimum is the most sensitive of the four methods and the peak-peak times are much less sensitive to a variation in input frequency. These results disagree with [6] who found the peak-peak times to be more frequency-dependant than the first arrival-based estimates.

Figure 19 and Table 3 summarize the variation in shear stiffness, G_{xy}, with confining pressure observed using the various measures of data interpretation outlined above. The slopes of the lines are the α values and these slope values are listed on Fig. 19. Excluding consideration of the phase versus frequency approach, which clearly gives unreasonable estimates of G, when the various methods are compared there are noticeable differences between the calculated G_{xy} and α values. The G_{xy} values are listed on Table 3, along with the relative error when the value is compared with the 2D FFT method. At each confining pressure, the standard deviations for the G_{xy} values were between 20 and 30 % of the mean G_{xy} value. For the α values (again excluding the phase versus frequency approach), the standard deviation was 11 % of the mean α value.

For the range of confining pressures considered, the point of inflection method gave the lowest ε^r values; this agrees with the observed proximity of the wave front arrival with this point [Figs. 4, 9 (*k*) and (*l*)]. The cross-correlation and the time domain contour plot methods gave G_{xy} values that were within 10 % of those predicted using the 2D FFT method, and the peak-peak method and inflection point had ε^r values that were <20 %. The first zero-crossing method $\varepsilon^r < 25$ % and the point of first local minimum have $\varepsilon^r > 40$ %. The phase versus frequency method under predicted G_{xy} by as much as 50 %. The first zero-crossing method consistently overestimated the system stiffness, while the peak-peak method underestimated G_{xy} at low confining pressures and overestimated G_{xy} at higher pressures. These results do not support the proposition by Yang and Gu [2] that the point of first local minimum is the most appropriate point for stiffness calculation, in fact, here the point of first local minimum can lead to over prediction of stiffness by over 40 %. Tables 4 and 5 present a similar scatter in the existing methods when compared to the 2D FFT.

8 Application: influence of contact model on $G - \sigma_0$ relationship

In geomechanical applications both the stiffness value and the observed relationship between the small-strain stiffness, G, and the mean effective stress, σ_0', are important. The $G-\sigma_0'$ relationship has been expressed often using a power law, i.e. $G \propto \sigma_0'^{\alpha}$, (e.g. [41] and [56]) and accurate quantification of α is important to predict soil response. Theoretical considerations, such as [41], give $\alpha = 1/3$, however experimental data on real soil tend to give α values between 0.4 and 0.5 (e.g. [56,57]). Yimsiri and Soga [58] analytically demonstrated that the $G - \sigma_0'$ relationship is affected by the form of the force–displacement relationship assumed at particle contacts. These earlier findings are extended here by considering wave propagation and using the three different contact models outlined above.

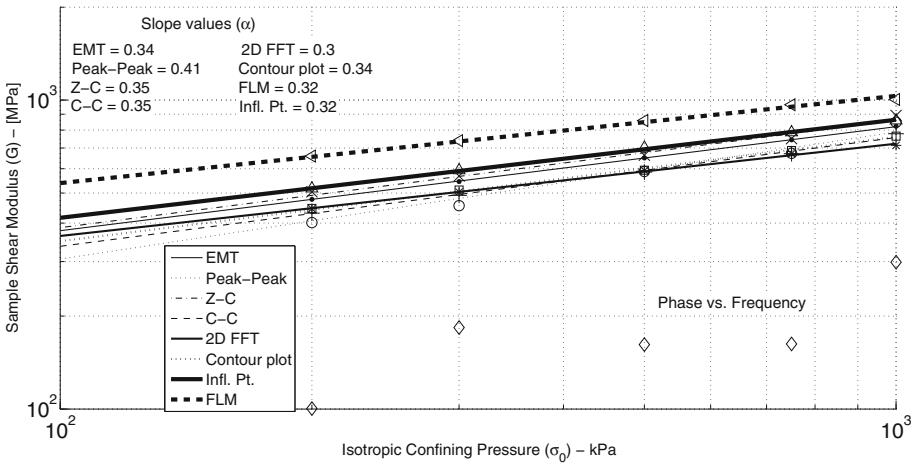

Fig. 19 Sample shear modulus, G_{xy}, versus isotropic confining stress, σ_0, obtained using different travel time determination techniques and effective medium theory (EMT)

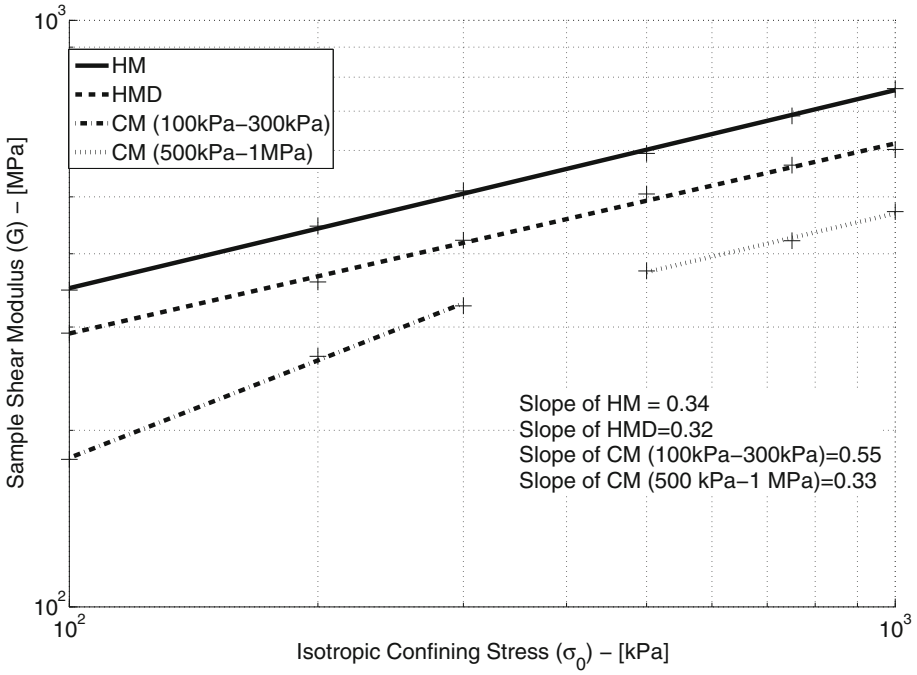

Fig. 20 Sample shear modulus, G, versus isotropic confining stress, σ_0, obtained for samples with different interparticle contact models using the two-dimensional fast Fourier transform travel time determination technique. Two slopes are calculated for Cavarretta–Mindlin contact model. The first considering the stress range 100–300 kPa and the second considering the stress range 500 kPa–1 MPa

Figure 20 illustrates the sensitivity of the system response to confining pressure for the three different contact models considered in this study. This is the first time that these contact models from the literature have been implemented in DEM and compared with each other to highlight their influence on the sample stiffness. In all cases the stiffness was determined using the 2D FFT method as this is considered to be the most reliable method. It is clear that use of the HMD model reduces the overall stiffness less than the cases where the CM model is used. Referring to Fig. 3a, b the CM model reduces the normal stiffness, and one would expect the normal component of the contact to have a greater influence than the tangential component. Using a micro-mechanics-based analytical approach [58] examined the sensitivity of the small-strain stiffness to the contact model used. Yimsiri and Soga also considered a rough-surface model (referring to [59]) and found a difference between the relationships between the confining stress and stiffness at low and high confining pressures. Taking the Yimsiri and Soga findings into account, the CM model gives a bi-linear type response with α being approximately 0.55 at stress levels below about 300 kPa and α being 0.33, i.e. the same as in the HM model, at higher stress levels. This is due to the contact model behaviour. Once the contact displacement exceeds a threshold value, which is a function of the hardness of the particle asperities and the roughness of the particle, the CM contact model behaves like the HM contact model. This further illustrates the influence of the interparticle contact model on the sample stiffness. As the sample with the CM contact model is less stiff, the travel times are longer and so the differences in travel times as a function of interpretive technique are more noticeable. This study isolates the effect of the contact model on the shear modulus versus con-

fining pressure relationship by using a monodisperse, lattice packed sample. Khidas and Jia [10] have shown that the relationship between shear wave velocity and confining pressure is influenced by anisotropy. The fabric considered here is cross-anisotropic and this may influence the exponent value. The nature of the simulation set-up excludes the influences of polydispersity and lack of sphericity, which have been highlighted by Somfai et al [60] and Goddard [57], amongst others.

9 Conclusions

This paper has documented an analysis of the response of a cubic sample of uniform spheres with a face-centred-cubic packing to a point source dynamic excitation using a three-dimensional discrete element model. An ideal system was created so that meaningful conclusions about interpretation of bender element test data could be developed. Despite the inherent idealizations of the model the system response, as observed using a model receiver is similar to what is observed in a bender element in a physical test. The DEM analysis generated a rich data set that exposed the complexity of the system response.

The complexity of the system response, even for this ideal material, inhibited easy interpretation of the particle-scale information. The most useful approach to examine the raw particle-scale data was to consider the variation in the displacements along the centre line in the time and with position and to interpret this data using a contour plot. Taking the axes of this plot to be time and position, the slope of the contours of particle displacement can be used to determine velocity, and hence travel time.

It proved useful to examine the response in the frequency domain. The frequency domain data clearly indicate the complex response characteristics one would expect for such a multiple degree of freedom system. Most notably there clearly is a filtering of the higher frequencies as the signal moves through the sample. The received signal is frequency dependent and it exhibits dispersion, suggesting that it is unlikely that simply picking a point on the received signal will provide an accurate or even reliable estimate of stiffness. The position of the geometric points on the time axis is a function of both sample stiffness and the amount of dispersion that has occurred. This reinforces the unreliability of such methods.

The two-dimensional fast Fourier transform (2D FFT) method was seen to give a robust estimate of the sample stiffness. This method has the strongest theoretical basis for accurately interpreting the shear wave speed as it considers both the temporal and spatial variation of the wave as it propagates. If the results are presented in the frequency domain with angular velocity plotted against wave number the slope represents wave speed. There is no subjectivity as was the case in the time domain contour plot where a particular contour must be selected to determine the slope. The shear stiffness calculated from the 2D FFT method was in close agreement with the shear stiffness calculated from the stress probe tests carried out on the sample. This method also gave values of arrival time that were close to the arrival time of the shear wave front obtained from the particle-scale data (particle velocities and rotations as observed in Figs. 8, 9). The reliability of the 2D FFT method is further supported by comparison with values obtained from a number of the analytical methods considered. The 2D FFT travel time determination method, the principle of virtual displacement and dispersion relation theory had not previously been used to calculate the wave speed in numerical bender element test simulations. For the other methods considered the G_{xy} values were found to vary with transmitted frequency indicating that their reliability is affected by the dispersion of the wave as it propagates.

The 2D FFT method cannot easily be implemented in the laboratory; however, it is useful as a benchmark with which the other travel time determination methods are compared. The peak-peak method, first zero-crossing method and cross-correlation methods were all found to under-predict the stiffness of the sample. The point of first local minimum and inflection point were found to over predict the sample stiffness. The phase versus frequency plot method gave very unreasonable estimates of the stiffness even when an input signal was cycled ten times to represent the continuous signals that are recommended. The time domain contour plot method, which also uses multiple spatial measurements of the sample response, was more reliable than the other methods; however, as with the 2D FFT method, it cannot easily be applied in the laboratory. None of the methods consistently agreed with each other or with the benchmark two-dimensional fast Fourier transform method. This should prompt much more critical assessment of the methods used to interpret bender element tests in the laboratory and for more experimental investigation of the spatial variation of propagating waves.

The particle scale data did not provide evidence to support a clear link between the shear wave arrival and any of the characteristic points on the received signal that have been adopted in laboratory studies to estimate travel time. It must be acknowledged that, when compared with the more robust 2D FFT method, the laboratory methods do occasionally give reasonable estimates of the stiffness. The lack of a clear correlation with the analytical stiffness estimates, the stress probes and the 2D FFT method combined with a poor link to particle-scale observations indicates that they are purely empirical and lack a rigorous scientific basis.

As an illustrative application, the 2D FFT method was used to examine the sensitivity of the overall stiffness to the

contact model used in the simulation. It was found that both the CM models and the HMD models had a measurable influence on G_{xy}, thus it may be the deviation of real materials from a Hertzian contact model that explains the fact that the exponent in the $G - \sigma_0$ relationship is not 1/3. The link between individual contact springs and sample stiffness is clear as the HMD and CM models simulate contact springs of lower stiffness and the resulting sample stiffness is also lower in magnitude. The simulations using the CM model confirmed the bi-linear variation in the $G - \sigma_0$ relationship when plotted on logarithmic axes. This reflects experimental observations and analytical work that sought to explain the deviation of real materials from Hertzian behaviour.

Acknowledgments The authors would like to acknowledge the financial support of the EPSRC through Grant EP/G064954/1. The authors would particularly like to acknowledge the support of our project collaborators at the University of Bristol who are Dr. Martin Lings, Dr. Erdin Ibraim, Mr. Simon Hamlin, and Dr. Ignazio Cavarretta (now at the University of Surrey).

References

1. Alvarado, G., Coop, M.R.: On the performance of bender elements in triaxial tests. Géotechnique **62**(1), 1–17 (2012)
2. Yang, J., Gu, X.: Shear stiffness of granular material at small strains: does it depend on grain size? Géotechnique **63**(2), 165–179 (2013)
3. Shirley, D., Hampton, L.: Shear wave measurements in laboratory sediments. J. Acoust. Soc. Am. **63**(2), 607–613 (1978)
4. Yamashita, S., Kawaguchi, T., Nakata, Y.: Interpretation of international parallel test on the measurement of Gmax using bender elements. Soils Found. **49**(4), 631–650 (2009)
5. da Fonseca, A., Ferreira, C., Fahey, M.: A framework interpreting bender element tests, combining time-domain and frequency-domain methods. Geotech. Test. J. **32**(2), 1–17 (2009)
6. Clayton, C.R.I.: Stiffness at small strain: research and practice. Géotechnique **61**(1), 5–37 (2011). doi:10.1680/geot.2011.61.1.5
7. Arroyo, M., Muir Wood, D., Greening, P.D.: Source near-field effects and pulse tests in soil samples. Géotechnique **53**(3), 337–345 (2003). doi:10.1680/geot.53.3.337.37277
8. Leong, E., Cahyadi, J., Rahardjo, H.: Simulating bender element tests using the distinct element method. Can. Geotech. J. **46**, 792–812 (2009). doi:10.1139/T09-026
9. Marketos, G., O'Sullivan, C.: A micromechanics-based analytical method for wave propagation through a granular material. Soil Dyn. Earthq. Eng. **45**, 25–34 (2013)
10. Khidas, Y., Jia, X.: Anisotropic nonlinear elasticity in a spherical-bead pack: influence of the fabric anisotropy. Phys. Rev. E **81**(2), 021303 (2010). doi:10.1103/PhysRevE.81.021303
11. Suwal, L.P., Kuwano, R.: Disk shaped piezo-ceramic transducer for P and S wave measurement in a laboratory soil specimen. Soils Found. **53**(4), 510–524 (2013). doi:10.1016/j.sandf.2013.06.004
12. Hazzard, J.F., Maxwell, S.C., Young, R.P.: Micromechanical modelling of acoustic emissions. Soc. Pet. Eng. 519–526 (1998)
13. Li, L., Holt, R.M.: Particle scale reservoir mechanics. Oil Gas Sci. Technol. **57**(5), 525–538 (2002). doi:10.2516/ogst:2002035
14. Mouraille, O., Mulder, W.A., Luding, S.: Sound wave acceleration in granular materials. J. Stat. Mech: Theory Exp. **07**(23), 1–15 (2006). doi:10.1088/1742-5468/2006/07/P07023
15. Xu, X., Ling, D., Cheng, Y.P., Chen, Y.: Micromechanical study on shear wave velocity of granular materials using discrete element methods. In: Wu, C.-Y. (eds.) Discrete Element Modelling of Particulate Media, pp. 255–263. Royal Society of Chemistry Publishing, Birmingham (2012)
16. O'Donovan, J., O'Sullivan, C., Marketos, G.: Two-dimensional discrete element modelling of bender element tests on an idealised granular material. Granul. Matter **14**(6), 733–747 (2012). doi:10.1007/s10035-012-0373-9
17. Gu, X., Yang, J.: A discrete element analysis of elastic properties of granular materials. Granul. Matter **15**(2), 139–147 (2013). doi:10.1007/s10035-013-0390-3
18. Rowe, P.: The stress-dilatancy relation for static equilibrium of an assembly of particles in contact. Proc. R. Soc. Sci. Ser A: Math. Phys. Sci. **269**(1339), 500–527 (1962)
19. Thornton, C.: The conditions for failure of a face-centered cubic array of uniform rigid spheres. Géotechnique **29**(4), 441–459 (1979). doi:10.1680/geot.1979.29.4.441
20. Mouraille, O., Luding, S.: Sound wave propagation in weakly polydisperse granular materials. Ultrasonics **48**, 498–505 (2008). doi:10.1016/j.ultras.2008.03.009
21. Santamarina, J.C., Cascante, G.: Stress anisotropy and wave propagation: a micromechanical view. Can. Geotech. J. **33**(5), 770–782 (1996). doi:10.1139/t96-102-323
22. Crampin, S.: A review of wave motion in anisotropic and cracked elastic-media. Wave Motion **3**, 343–391 (1981)
23. Itasca Consulting Group: PFC3D Version 4.0 User Manual, Itasca Consulting Group, Minneapolis (2007)
24. Cundall, P.A., Strack, O.D.L.: A discrete numerical model for granular assemblies. Géotechnique **29**(1), 47–65 (1979). doi:10.1680/geot.1979.29.1.47
25. Cundall, P.A., Strack, O.D.L.: The distinct element method as a tool for research in granular media. Report to the National Science Foundation (1979)
26. Cavarretta, I., O'Sullivan, C., Ibraim, E., Lings, M., Hamlin, S., Muir Wood, D.: Characterization of artificial spherical particles for DEM validation studies. Particuology **10**(2), 209–220 (2012). doi:10.1016/j.partic.2011.10.007
27. Thornton, C., Randall, C.: Applications of theoretical contact mechanics to solid particle system simulation. In: Satake, M., Jenkins, J.T. (eds.) Micromechanics of Granular Materials, pp. 133–142. Elsevier (1988)
28. Thornton, C., Yin, K.: Impact of elastic spheres with and without adhesion. Powder Technol. **65**, 153–166 (1991)
29. Cavarretta, I., Coop, M.R., O'Sullivan, C.: The influence of particle characteristics on the behaviour of coarse grained soils. Géotechnique **60**(6), 413–423 (2010). doi:10.1680/geot.2010.60.6.413
30. Mindlin, R.D., Deresiewicz, H.: Elastic spheres in contact under varying oblique forces. J. Appl. Mech. **20**, 327–344 (1953)
31. Johnson, K.: Contact Mechanics. Cambridge University Press, Cambridge (1985)
32. Hamlin, S.: Experimental Investigation of Wave Propagation through Granular Material, PhD thesis (in preparation), University of Bristol (2014)
33. Hardy, S.: The Implementation and Application of Dynamic Finite Element Analysis to Geotechnical Problems, PhD thesis, Imperial College London (2003)
34. Jovičić, V., Coop, M.R., Simić, M.: Objective criteria for determining Gmax from bender element tests. Géotechnique **46**(2), 357–362 (1996). doi:10.1680/geot.1996.46.2.357
35. Judge, J.A., Houston, B.H., Photiadis, D.M., Herdic, P.C.: Effects of disorder in one- and two-dimensional micromechanical resonator arrays for filtering. J. Sound Vib. **290**(3–5), 1119–1140 (2006). doi:10.1016/j.jsv.2005.05.003
36. O'Donovan, J.: Micromechanics of Wave Propagation through Granular Material, PhD thesis, Imperial College London (2013)

37. Lee, J.-S., Santamarina, J.C.: Bender elements: performance and signal interpretation. J. Geotech. Geoenviron. Eng. **131**(9), 1063–1070 (2005). doi:10.1061/(ASCE)1090-0241(2005)131:9(1063)
38. Sanchez-Salinero, I., Rosset, J.M., Stokoe II, K.H.: Analytical studies of body wave propagation and attenuation. In: University of Texas, p. Rep. No. GR-86-15 (1986)
39. Arroyo, M., Muir Wood, D., Greening, P.D., Medina, L., Rio, J.: Effects of sample size on bender-based axial G0 measurements. Géotechnique **56**(1), 39–52 (2006). doi:10.1680/geot.2006.56.1.39
40. Ferreira, C., da Fonseca, A.: International Parallel Tests on Bender Elements at the University of Porto, Portugal (2005)
41. Duffy, J., Mindlin, R.D.: Stress–strain relations and vibrations of a granular medium. ASME J. Appl. Mech. **24**, 585–593 (1957)
42. Greening, P.D., Nash, D.F.T.: Frequency domain determination of G0 using bender elements. Geotech. Test. J. **72**(3), 1–7 (2004). doi:10.1520/GTJ11192
43. Lawney, B.P., Luding, S.: Frequency filtering in disordered granular chains. Acta Mech **225**(8), 2385–2407 (2014)
44. De Mol, L.: Wave Propagation in Granular Material: Theoretical and Numerical Analysis in Comparison to Experimental Data, MSc dissertation, Ruhr-University Bochum (2013)
45. Chang, C., Liao, C.L.: Constitutive relation for a particulate medium with the effect of particle rotation. Int. J. Solids Struct. **26**(4), 437–453 (1990). doi:10.1016/0020-7683(90)90067-6
46. Kruyt, N.P., Agnolin, I., Luding, S., Rothenburg, L.: Micromechanical study of elastic moduli of loose granular materials. J. Mech. Phys. Solids **58**, 1286–1301 (2010). doi:10.1016/j.jmps.2010.06.003
47. Santamarina, J., Klein, A., Fam, M.A.: Soils and Waves: Particulate Materials Behavior, Characterization and Process Monitoring. Wiley, Chicester, UK (2001)
48. O'Sullivan, C.: Particulate Discrete Element Modelling—A Geomechanics Perspective. Taylor and Francis, New York (2011)
49. Marketos, G., Bolton, M.: Flat boundaries and their effect on sand testing. Int. J. Numer. Anal. Methods Geomech. **34**, 821–837 (2010). doi:10.1002/nag
50. Lings, M.L.: Cubic Anisotropy, Personal Communication. University of Bristol, Bristol (2013)
51. Norris, A.N.: Poisson's ratio in cubic materials. Proc. R. Soc A: Math. Phys. Eng. Sci. **462**(2075), 3385–3405 (2006). doi:10.1098/rspa.2006.1726
52. Walton, K.: The effective elastic moduli of a random packing of spheres. J. Mech. Phys. Solids **35**(2), 213–226 (1987)
53. Mouraille, O.: Sound propagation in dry granular materials?: discrete element simulations, theory, and experiments, PhD thesis, University of Twente (2009)
54. Merkel, A., Tournat, V., Gusev, V.: Experimental evidence of rotational elastic waves in granular phononic crystals. Phys. Rev. Lett. **107**(22), 225502 (2011). doi:10.1103/PhysRevLett.107.225502
55. Merkel, A., Tournat, V., Gusev, V.: Dispersion of elastic waves in three-dimensional noncohesive granular phononic crystals: properties of rotational modes. Phys. Rev. E **82**(3), 031305 (2010). doi:10.1103/PhysRevE.82.031305
56. McDowell, G., Bolton, M.: Micro mechanics of elastic soil. Soils Found. **41**(6), 147–152 (2001)
57. Goddard, J.D.: Nonlinear elasticity and pressure-dependent wave speeds in granular media. Proc. R. Soc. Sci. Ser A: Math. Phys. Sci. **430**, 105–131 (1990). doi:10.1098/rspa.1990.0083
58. Yimsiri, S., Soga, K.: Micromechanics-based stress-strain behaviour of soils at small strains. Géotechnique **50**(5), 559–571 (2000). doi:10.1680/geot.2000.50.5.559
59. Greenwood, J.A., Tripp, J.H.: The elastic contact of rough spheres. J. Appl. Mech. **34**(1), 153–159 (1967)
60. Somfai, E., Roux, J.N., Snoeijer, J.H., van Hecke, M., van Saarloos, W.: Elastic wave propagation in confined granular systems. Phys. Rev. E **72**(2), 021301–021321 (2005)